

<https://doi.org/10.1038/s44334-025-00028-x>

Rapid data acquisition and machine learning-assisted composition design of functionally graded alloys via wire arc additive manufacturing

Xin Wang^{1,3}, Soumya Sridar^{1,3}, Michael Klecka² & Wei Xiong¹ ✉

The lack of high-quality datasets in materials science hinders artificial intelligence (AI)-driven alloy design. To address this challenge, wire arc additive manufacturing (WAAM) was employed to fabricate graded alloys, generating extensive data for machine learning (ML)-assisted property prediction. ML models were developed using high-throughput experiments, computational models, and genetic algorithm to optimize feature selection, successfully predicting hardness and porosity. The ML model demonstrated its efficacy by designing a gradient alloy with enhanced properties. However, scaling up revealed uncertainties in tensile property and porosity due to differences in size and thermal conditions between the designed alloy build and the gradient print used to construct the ML model. This underscores the need for uncertainty quantification and process optimization in WAAM-driven alloy design. Our work advances AI-integrated additive manufacturing, offering a rapid approach to exploring process–structure–property relationships and accelerating materials development.

The machine learning (ML) method, which maps the relationship between the property of interest and materials descriptors, has gained significant attention due to its ability to expedite numerical simulations and facilitate the materials design^{1,2}. The approach proves valuable for alloy development and materials property prediction in the vast composition space^{3–9}. Nonetheless, the scarcity of robust databases constrains the widespread adoption of ML within the materials community¹⁰. To surmount these limitations and unlock the full potential of ML in materials discovery and design, concerted efforts must be directed toward the acquisition of high-quality databases. Compiling a substantial and reliable database pose challenges due to the scarcity of comprehensive data in literature. Furthermore, variations in materials processing and property testing conditions across publications introduce noise and diminish the quality of the available data. Consequently, the construction of a high-quality database necessitates the implementation of high-throughput experiments, and various methodologies have been developed to fulfill this purpose. Magnetron sputtering can map several compositions in thin-film form, while it cannot be used for producing bulk samples with more representative characteristics, such as mechanical properties and corrosion resistance^{11–13}. The development of diffusion couples or multiples has a long-standing history^{14,15}, offering an effective and

feasible approach for investigating phase diagrams and exploring composition–process–microstructure–property relationships¹⁶. Nevertheless, the determination of element distribution is inherently tied to their respective diffusivities, posing challenges in achieving the desired composition. Additionally, the limited size of the diffusion zone often hinders the direct deduction of bulk properties^{17–19}.

Additive manufacturing (AM)^{20–23} revolutionizes the fabrication of components by layer-by-layer material deposition, enabling rapid construction of near-net-shape geometries and the development of compositionally graded materials. Such capabilities, unparalleled by other high-throughput processing techniques, hold the promise of a paradigm shift in the efficient screening of alloy compositions²⁴. In comparison to alternative additive manufacturing techniques like laser powder bed fusion²⁵, directed energy deposition²⁶, and electron beam freeform fabrication²⁷, wire arc additive manufacturing (WAAM) has demonstrated notable advantages^{28–30}. These include cost reduction through the utilization of wire instead of powder (which can be up to three times more expensive) and higher deposition rates^{31,32} for the fabrication of large-sized builds^{33,34} with near net shape. Compared with the powder-bed process, wire feed has higher material usage efficiency with up to

¹Physical Metallurgy and Materials Design Laboratory, Department of Mechanical Engineering and Materials Science, University of Pittsburgh, Pittsburgh, PA, 15261, USA. ²RTX Technology Research Center, 411 Silver Lane, East Hartford, CT, 06108, USA. ³These authors contributed equally: Xin Wang, Soumya Sridar.

✉ e-mail: weixiong@pitt.edu

100% of the wire material deposited into the component³⁵. Additionally, due to the existing welding techniques, wires are lower in cost and readily available than alloy powders as the feedstock materials, making wire-feed technology more cost-competitive. In contrast to the low energy efficiency of laser-based processes (ranging from 2% to 5%)³⁶ and electron beam processes (ranging from 15% to 20%)³⁷, arc welding techniques such as gas metal arc welding (GMAW), gas tungsten arc welding (GTAW), or plasma-arc welding (PAW) can achieve energy efficiencies of up to 90%³⁸.

A second challenge in constructing ML models lies in the selection of suitable material descriptors to predict the desired property. Typically, the ML approach involves establishing a surrogate model f that discerns the connection between the property of interest Y and a series of material descriptors X . Consequently, the effectiveness and precision of the ML prediction are contingent upon the chosen model f and material descriptors X . To ensure robust and accurate predictions, it becomes imperative to amass an extensive collection of “good” descriptors and curate the appropriate set for analysis. When it comes to gathering “good” descriptors, computational tools offer the potential to augment the limited experimental data by introducing additional physics-based features into the analysis^{39,40}. However, given the multitude of descriptors derived from both experimental and simulation sources, the quest for an effective method to select an optimal descriptor recipe becomes essential. The sheer number of possible descriptor combinations, which grows exponentially with the number of descriptors (n), renders a brute-force inspection impractical, with a total of $2^n - 1$ choices for the descriptor recipe^{10,41}. To overcome this challenge, genetic algorithms (GA) emerge as a powerful tool. Mimicking the evolutionary principles of “natural selection” and “survival of the fittest”⁴², GA is capable of efficiently sifting through the extensive pool of collected descriptors. By leveraging GA, the most appropriate material descriptors can be selected and thus enhance the model’s performance through judicious feature selection. CALPHAD (Calculation of Phase Diagrams)⁴³ is a reliable shortcut to determine the phase equilibria and thermodynamics of multicomponent systems. High-throughput CALPHAD calculations can be employed for deducing the thermodynamic properties in a large composition domain that are complex, expensive, and time-consuming to be determined using experiments. This makes it an efficient method for generating the material descriptors for GA.

This study presents a design framework that integrates WAAM, the CALPHAD approach, and GA to establish a ML model aimed at the design of a new alloy. Specifically, our focus lies in the development of functionally graded materials obtained through the printing process, employing P91 steel and Inconel 740H (denoted as 740H hereafter) superalloy as the base materials^{44,45}. As shown in Fig. 1, the initial step of our investigation entails

the utilization of WAAM to fabricate a wall-shaped sample, gradually transitioning from pure P91 steel to 740H superalloy in 10 wt.% increments. Subsequently, we employed a comprehensive suite of characterization techniques, including hardness testing, SEM imaging, and composition measurements, along three distinct tracks spanning from the P91 side to 740H in the left, middle, and right of the sample. Each track comprised 145 data points, yielding a total of 435 SEM images (about an area of 7000 μm^2) along with corresponding hardness and composition measurements at various locations. In addition to these measurements, properties such as phase fractions and thermodynamic characteristics were calculated to further augment the database depth and richness. GA was performed for exploration of the dataset, pinpointing the most influential features capable of accurately predicting hardness and porosity. Subsequently, armed with this optimized model the alloy design was conducted by blending 740H superalloy and P91 steel during a twin-wire feed AM, two materials known for their excellent as-built properties. The resultant alloy was constructed and subjected to systematic characterization. The outcomes demonstrate the remarkable accuracy of our model, with the designed alloy exhibiting exceptional as-built properties, attesting to the efficiency and efficacy of our alloy design framework. It is worth noting, however, that the thermal history and location-specific properties inherent in large-scale AM builds introduce an element of uncertainty in WAAM prints, necessitating their important consideration in future endeavors aimed at quantifying quality.

Results

Characterization and CALPHAD modeling of linear gradient sample

Figure 2 illustrates the gradual compositional transition, as measured by EDS, from P91 steel to 740H superalloy in the gradient build depicted in Fig. 1. This spatial variation in composition yields a distinctive set of experimental data with unique compositions. Notably, there exists a favorable correlation between the measured composition and the nominal composition of the graded alloy, affirming the efficacy of composition control achievable through the implementation of a twin-wire feeder in WAAM.

In Fig. 3, three distinct tracks from the builds exhibit diverse properties and microstructures at equivalent distances along the build direction. This high-throughput experimentation elucidates the evolution of structure and properties in response to varying compositions, which can be explicated as follows: The hardness initially experiences an increase followed by a sudden decrease (Fig. 3b) due to the transition of the matrix from the martensite to austenite phase (Fig. 3g, h). As depicted in Fig. 3d, the porosity displays a random pattern along the build direction, suggesting its independence from composition. However, the presence of more black dots (Track 1) signifies higher porosity, indicating a potential sensitivity of porosity to the location

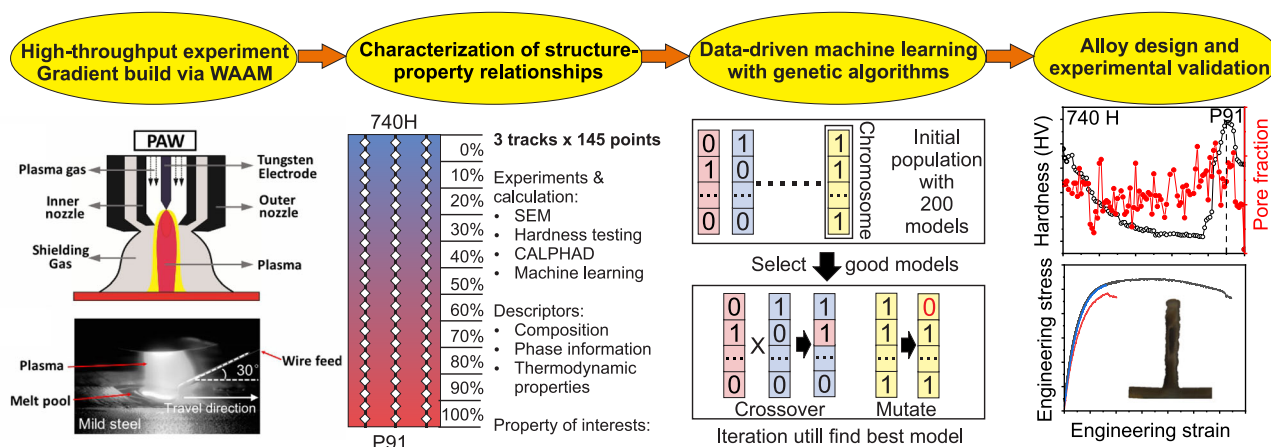


Fig. 1 | Flow chart of the proposed work. First, build the gradient alloy block using WAAM. Second, measure the hardness, porosity, cracks, and compositions and use different modeling tools to build the database for the ML model. Third, optimize

descriptor selection using a genetic algorithm. Lastly, predict the gradient alloy property, verify the design using experiments, and discover the location-specific properties.

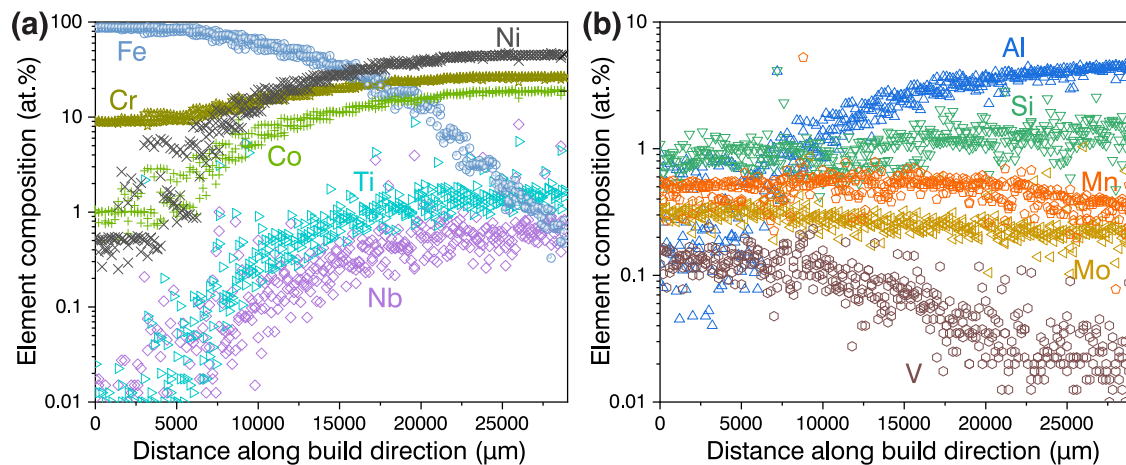


Fig. 2 | Element distribution along with the gradient build. a Fe, Ni, Cr, Co, Ti, and Nb; **(b)** Al, Si, Mn, Mo, and V.

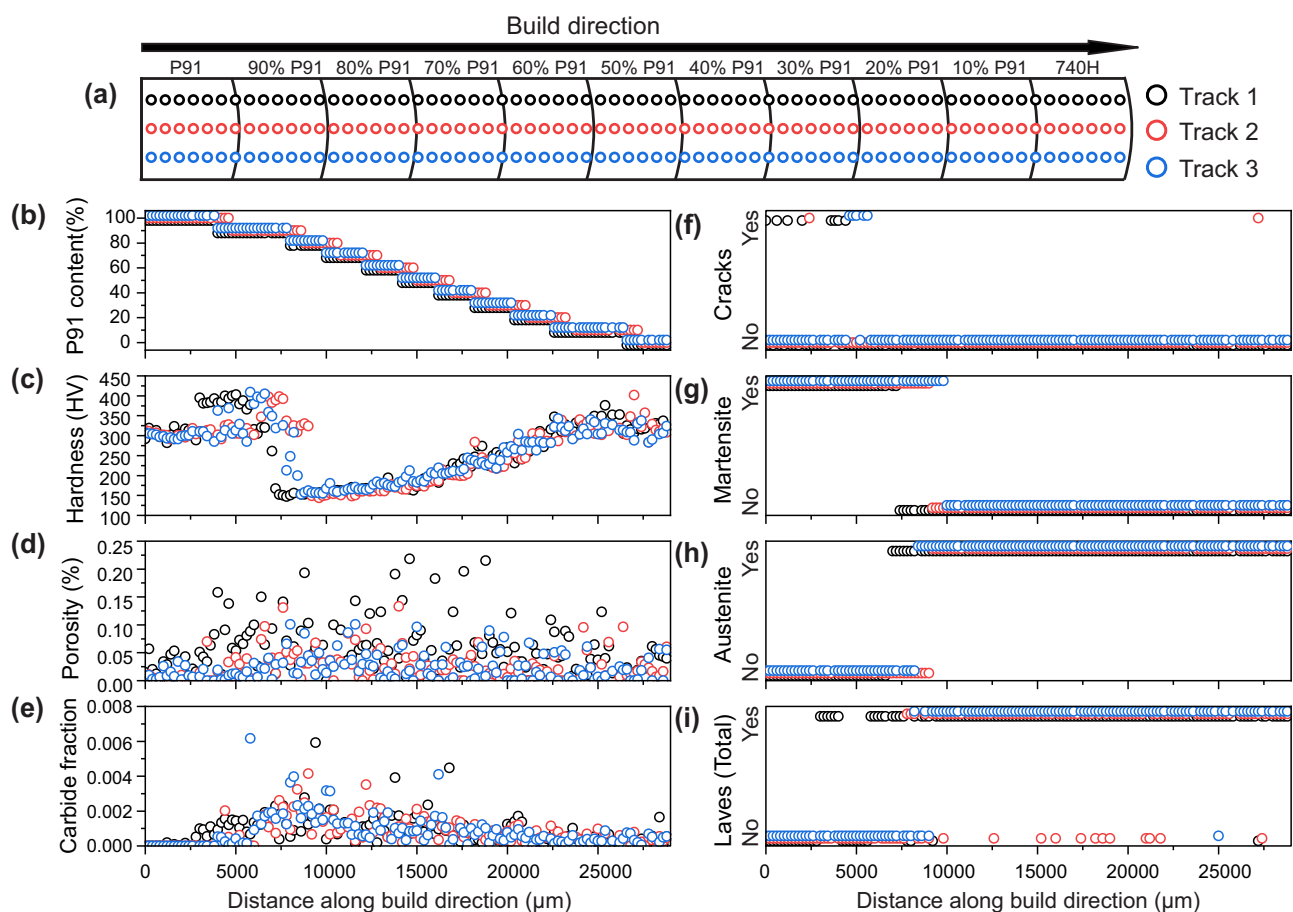


Fig. 3 | High throughput experimental results along build direction. a Schematic of the build and three testing tracks **(b)** P91 content, **(c)** Vickers hardness, **(d)** Porosity, **(e)** carbide fraction, **(f)** If cracks are introduced during hardness test, **(g)** Martensite distribution, **(g)** Austenite distribution, **(i)** Laves phase distribution.

perpendicular to the build direction. The carbide fraction exhibits an initial increase followed by a subsequent decrease (Fig. 3e), analogous to CALPHAD calculations conducted utilizing the Scheil module of Thermo-Calc software (refer to Supplementary Fig. S1). In Fig. 1g, h, the matrix undergoes a transformation from martensite to austenite when the building distance reaches 10,000 μm , which aligns with the predicted M_s temperature (refer to Supplementary Fig. S2). This congruity between experimental observations and simulations substantiates the accuracy of the simulation in capturing material properties and structure, thereby validating the utilization of the calculated results as material descriptors.

ML model aided by genetic algorithms

Material models are only as good as the descriptors they are built on. In this work, additional descriptors were calculated in addition to experimentally measured chemical composition, including phase fractions, thermodynamic properties, and M_s temperature, etc. These calculated descriptors proved essential since incorporating them showed dramatically lower error than those relying on composition alone (Fig. 4). Genetic algorithms were repeatedly applied to select the most informative descriptors and refine our models. With each iteration, the models improved, until reaching an optimal plateau within 40 iterations. The algorithms effectively identified the

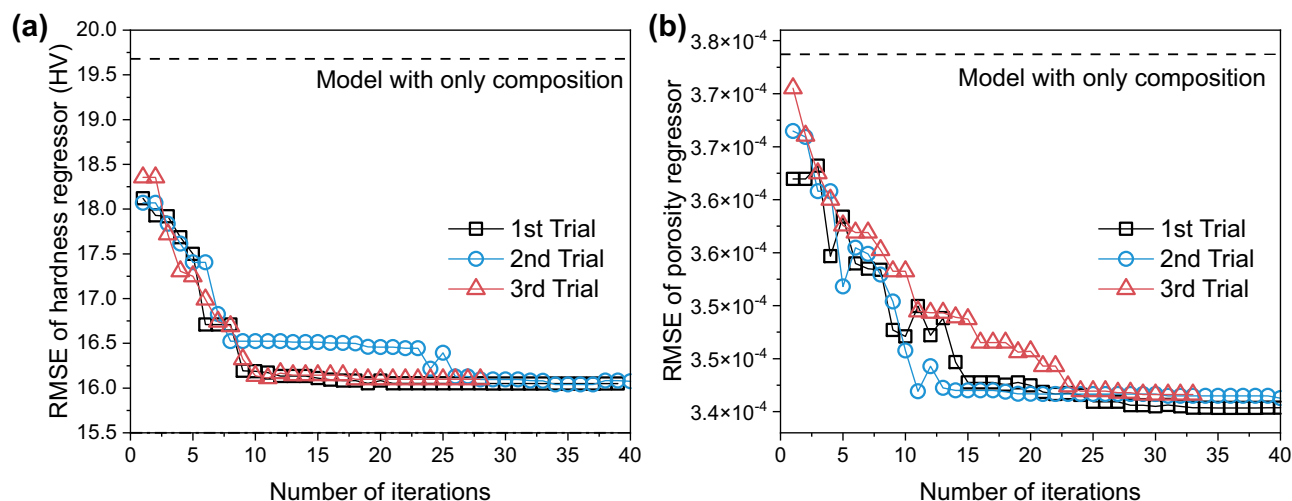


Fig. 4 | The model performance as a function of genetic algorithms iterations. a Hardness model, **(b)** porosity model. The dashed line is the model trained with only alloy composition, while the colored lines are models trained with the composition and calculated descriptors.

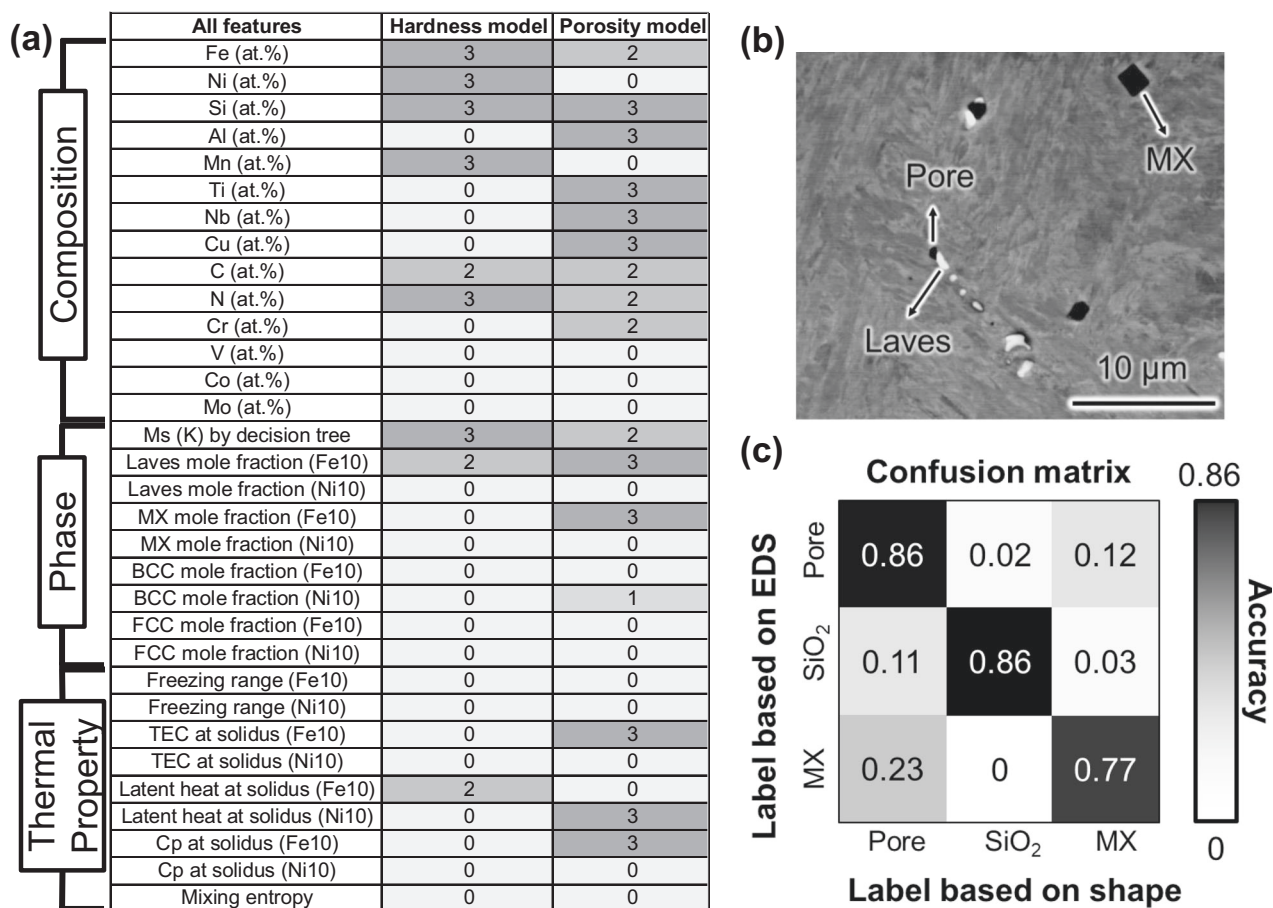


Fig. 5 | Evaluation of the GA-selected features. a Materials properties selected by GA models the numbers denote the number of times the feature has been selected by GA during the three trials. Fe10 and Ni10 denote features calculated using TCFE10

and TCNI10 databases, respectively. **b** SEM image showing the Laves phase and the pore close to it. **c** Confusion matrix showing the relationship labeling accuracy based on more than 140 black features in SEM images.

most effective descriptor set to explain hardness and porosity. All three genetic algorithms tests performed similarly, indicating the algorithms can search the space of possibilities to find the best descriptor combinations.

The automated feature selection approach using GA, enables the identification of the most informative descriptors that yield the smallest prediction error, shedding light on the potential physical connections

between these descriptors and the target properties. Fig. 5a concisely summarizes the frequency of feature selection in the GA-derived descriptor sets across three trials. Notably, in the hardness model, features such as the composition of Fe, Ni, Si, Mn, N, Martensite, and Laves phase fractions, as well as the latent heat at the solidus temperature, have been selected more than twice. Similarly, the porosity model highlights the repeated selection of

features including the composition of Si, Al, Ti, Nb, Cu, Laves and MX phase fractions, as well as thermal properties like the TEC, latent heat, and heat capacity (C_p).

The GA's feature selection process offers valuable insights into the relationship between these features and the properties of interest with some of these relationships being confirmed by literature. For example, Al and Ti were selected 3 times for porosity prediction, indicating their content have an impact on the porosity. This finding aligns with Panwisawas et al.⁴⁶ who reported that lower Ti and Al content could increase both dynamic viscosity and thermal conductivity in superalloys which leads to more stagnant fluid flow during additive manufacturing and consequently lower porosity. Additionally, TEC, latent heat, and heat capacity emerged as important features for predicting porosity. Due to the layer-by-layer nature of WAAM, there is a temperature gradient between layers. This temperature difference combined with a high TEC, results in substantial thermal contraction and the generation of residual stresses, which can exceed the local strength of the material and form microcracks⁴⁷. Furthermore, latent heat and heat capacity are key parameters in analytical models for thermal distribution, melt pool geometry, temperature and velocity field calculations⁴⁸ that could further impact on the pore formation^{46,49}.

In the meantime, GA also guides us to uncover insights worth exploring. For instance, further investigation revealed the significance of Laves and MX phases in porosity prediction. Fig. 5b demonstrates that the co-presence of Laves phase and pore. This is possible due to that Laves phases typically forms in the interdendritic region at the end of solidification⁵⁰. If it is in conjunction with inadequate transformation of liquid to solid, this can result in the development of localized regions of porosity within the interdendritic region, which leading to the co-presence of Laves phase and pores. Fig. 5c is the confusion matrix to describe the accuracy of our model labeling in phase based on the black feature shape, and it reveals the limitations of our method in distinguishing between pores and MX phases. During the SEM image analysis black feature is labeled as SiO_2 if the shape was very large, it is labeled as carbides if it showed a sharp edge, and it is pore if it had a rounded or complex shape. Then we took more than 100 black features and measured their composition using EDS to what are the true phases. In the analysis, if the black feature has the matrix composition it is the pore; it is SiO_2 if the Si content is high; it is carbide if it has high Nb/Ti content. Based on the first row, 86% of pores were labeled as pores based on shape, 2% of pores were mislabeled as SiO_2 , and 12% of pores were mislabeled as MX carbides. Although it identifies 86% of pores, it occasionally mislabels MX phases as pores, resulting in a correlation between porosity and MX phase fraction. It is to be noted that the SiO_2 particles can be either those stuck to the sample surface during the last step of polishing and remains stuck even after sonification or due to the Si in the feedstock which serves as deoxidizers and form SiO_2 during printing. These findings underscore the role of GA in discerning the relevance of materials descriptors to the target properties, thereby enhancing model performance.

Furthermore, the selection of an appropriate thermodynamic database holds paramount importance when designing gradients between dissimilar materials. Here, features were calculated using the TCFE10 and TCNI10 databases, and intriguingly, GA consistently favors the results derived from the TCFE10 database over the TCNI10 database. This preference suggests that the TCFE10 database offers greater utility in modeling hardness and porosity within the scope of this study.

Models were constructed utilizing GA-selected features to predict the hardness and porosity, employing a linear gradient composition spanning from 740H superalloy to P91 steel (Fig. 6). The projected hardness exhibits a gradual decrease upon the composition gradient from P91 steel to 740H superalloy. However, once reaching an 80 wt.% P91 composition, the hardness experiences a dramatic surge, peaking at approximately 400 HV, and subsequently declines as the composition nears pure P91. Moreover, the porosity shows a less smooth change along with the change of P91 content. This is due to the porosity dependent on features like heat capacity and the thermal expansion coefficient (TEC), which vary non-linearly with the P91 content (Supplementary Fig. S3c, d). Nevertheless, the porosity shows a

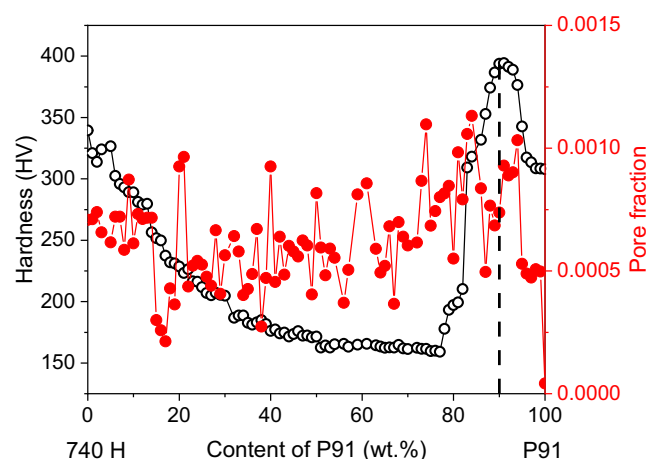


Fig. 6 | ML predicted hardness and porosity for compositionally gradient alloy from 740H superalloy to P91 steel. The red line represents pore fraction prediction, and the black dot line is the predicted hardness.

relatively low value of about 0.007 near the hardness peak region. Thus, by employing ML models, the 90 wt.% P91 alloy emerges as a promising candidate for the WAAM manufacturing method, boasting relatively low porosity and high hardness as shown in Fig. 6.

Evaluation of the design alloy and its location specific structure and properties

Consequently, a 90% P91 sample was fabricated, possessing dimensions of 190 mm length, 15 mm width, and 105 mm height (Fig. 7a)). To investigate property and microstructure variations along the build direction, eight locations were chosen from the bottom to the top of the build, aligning with the build direction.

Figure 7b, c reveals a martensitic microstructure, wherein the prior austenite grains exhibit an increasing trend in size from the bottom to the top of the build. The main reason for the smaller prior austenite grains in the bottom portion is because of the effective heat dissipation by the mild steel substrate with high thermal conductivity leading to higher cooling rate. As the build height increases, the previously deposited material which is at higher temperature will act as the substrate for the newly deposited material and hence, will have lower cooling rate, leading to larger prior austenite grain size. Among the available techniques, indentation testing stands out as a particularly suitable method for characterizing the mechanical properties of compositionally-graded specimens⁵¹, as it correlates with both the 0.2% proof stress and the ultimate tensile strength⁵². Therefore, hardness mapping was employed to investigate the distribution of hardness throughout the build. As depicted in Fig. 7d, the measured hardness is 369.6 ± 20.3 HV, which is in close agreement with the predicted hardness of 393.7 HV, proving the model trained based on data obtained from small gradient sample (25 mm gradient section) can be used to predict the hardness of large 90 wt.% P91 build (105 mm in height). Nonetheless, the hardness exhibits significant variation, ranging from 207 to 416 HV. Notably, within the middle region of the build, there are numerous areas with low hardness, represented by blue and green colors. Such occurrences may be attributed to the indents encountering a pore. The high hardness regions (red islands) in the hardness map could possibly be regions with the hard MX phase. This observation underscores the non-uniform distribution of hardness or porosity along the build.

To further investigate the performance of the designed alloy, three tensile tests were performed and the microstructure of the 90 wt.% P91 alloy in as-built condition was characterized. Based on Fig. 8a, there is a significant variation in the performance of the sample cut from the WAAM build alloy. For test 1, it shows a yield strength of 873 MPa, tensile strength of 1086 MPa and elongation of 6.46% in the as-built condition. The yield strength are higher than the austenized and tempered P91 (475 MPa)

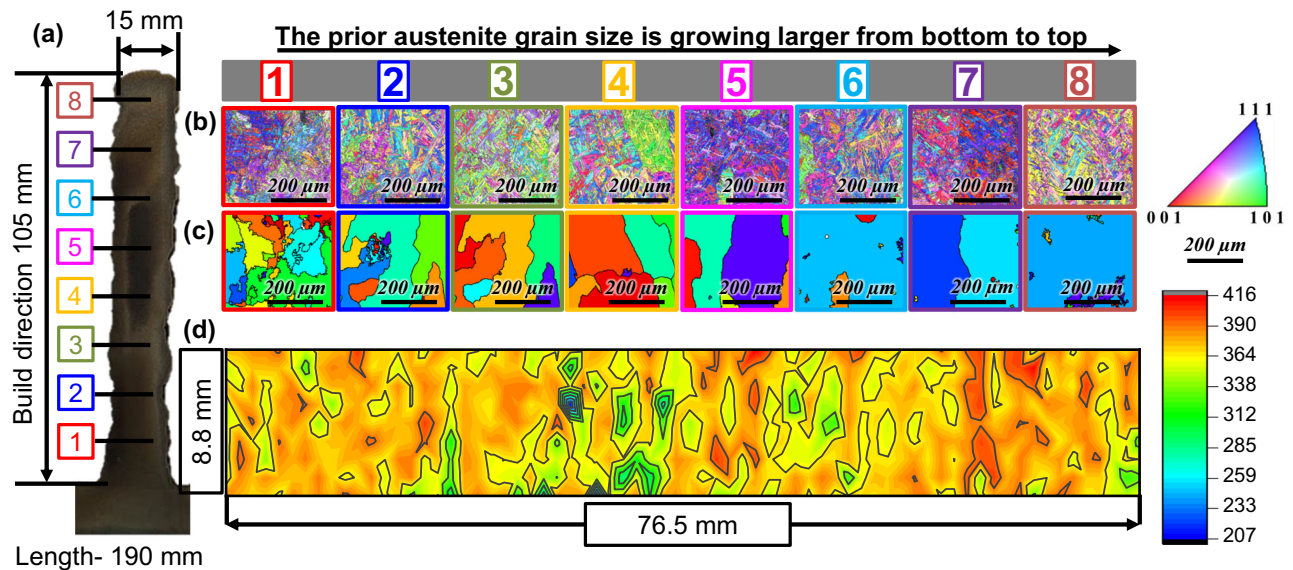


Fig. 7 | Build and characterize the designed 90 wt.% alloy. **a** Photo of the WAAM manufactured 90 wt.% P91 sample, **(b)** EBSD image along the build direction, **(c)** prior austenite reconstructed for **(b)**, and **(d)** hardness map of the manufactured sample.

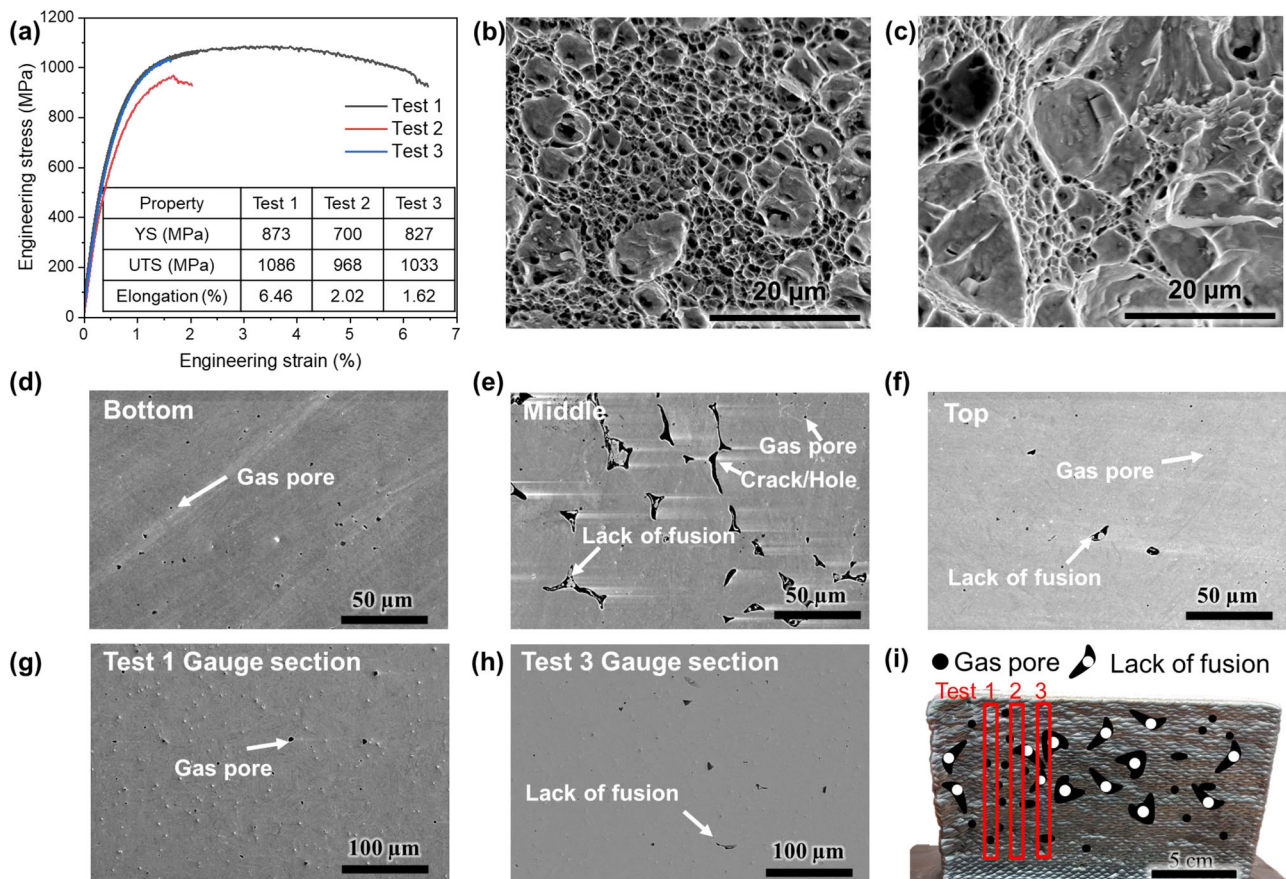


Fig. 8 | Uncertainty of the tensile property and microstructure of as-built 90 wt.% P91 alloy. **a** Uniaxial tensile stress-strain curves of as-built samples. **b** SEM image of the test 1 fracture, **(c)** SEM image of the test 3 fracture, SEM image showing the difference of

porosity at **(d)** bottom, **(e)** middle, **(f)** and top of the 90% P91 build, SEM image using secondary electron of the **(g)** test 1, **(h)** test 3 gauge length part of the 90% P91 build, and **(i)** schematic showing the variation of pores at different locations.

reported by Pandey et al.⁵³, yet slightly lower than the as-quenched P91 (900 MPa). Meanwhile, the 90 wt.% P91 build also exhibits higher strength compared to as-built (529 MPa) and heat-treated (710 MPa) 740H reported by Hu et al.⁵⁴ as well as welded 740 H (620 MPa)⁵⁵. Additionally, when comparing our gradient builds to other dissimilar compositions⁵⁶, our yield

strengths are generally higher, albeit with different elongation values. This demonstrates the effectiveness of our gradient design via hardness modeling in achieving high strength.

However, the ductility of our sample is a half or one third of the P91 and 740H reported in literature, and test 2 and 3 shows even worse ductility.

Based on the fracture surface, it was clear that more dimples were found in the test 1 sample (Fig. 8b) indicating a ductile mode of fracture compared with the fracture surface (Fig. 8c) from test 3 which showed more cleavages denoting brittle mode of fracture.

For probing the reason behind this observation, SEM imaging was performed to check the porosity. Fig. 8d–f shows the porosity variation along the build direction. The bottom and top part showed small spherical gas pores, which is caused due to the trapped gas⁵⁷. The porosity is 0.001 which is close ML model predicted porosity of 0.007, indicating a good accuracy of the ML model. However, the lack of fusion pores is noticeably observed in the middle part and the porosity increased to 0.0267 due to the input heat source energy that fails to fully melt the materials and leaves large and irregular voids⁵⁸. Such porosity distribution is in accordance with the hardness map in Fig. 7d, which shows the middle of the build has more low hardness area. The sharp edges of these large pores in the middle can act as stress raisers during the tensile testing leading to premature cracking. Moreover, the cracks and pores may also be caused by the localized residual stress during the cyclic heating and cooling process⁵⁹. Fig. 8g, h show the porosity variation at the gauge section of the tensile test. As summarized in Fig. 8i, there are more cracks, pores, and lack of fusion in the middle portion of the sample compared with the top, bottom, left edge, and right edge. And test 1 has better properties because it has lesser pores of spherical shape in the gauge section. Since high porosity will decrease the ductility and strength⁶⁰, the significant difference in tensile property can be attributed to the varying site-specific porosity in the large single composition build (105 mm in height). On the contrary, the smaller linear gradient block that we built for data generation (25 mm in height), only shows lack of fusion pores in 4 out of 61 SEM images within the 90 wt.% P91 section. This disparity in the lack of fusion pore occurrence suggests that the printability characteristics of the middle section of larger builds differ from the AM build with smaller size. Generally, the influencing factors of printability and porosity can be categorized either into thermal or material intrinsic property aspects. Since the build has the same composition, the difference is caused by thermal profile variation at different locations of the build given the same printing parameters. As a result, the impact of the location-specific thermal profile and its impact on the properties should be considered in future work.

Discussion

This study addresses the limited availability of high-quality datasets, a challenge that has historically hindered the application of ML in materials science. By integrating WAAM, the CALPHAD method, and genetic algorithms, we present a rapid and efficient approach to exploring process-structure-property relationships and accelerating alloy development.

- WAAM was utilized to fabricate gradient alloys with controlled compositions, generates extensive datasets containing bulk material property and structure that are ideal for ML analysis.
- The genetic algorithm identifies key material descriptors, selecting the most relevant properties and structural factors influencing hardness and porosity. By leveraging these optimized features and database built using WAAM, the ML models achieve low errors (16 HV for hardness and 0.00034 RMSE for porosity), making them suitable for guiding alloy design.

- By applying the ML model, a 90 wt.% P91 alloy was designed to exhibit favorable mechanical properties in its as-built state which aligns with the ML prediction.
- Variation in porosity across different locations in large 90 wt.% P91 samples was observed, which reduced the strength and ductility. The porosity at bottom part agrees with ML prediction while the middle parts show large discrepancies. This highlights that though this approach could identify promising alloy while additional process optimization is needed to enhance ductility and reduce porosity, particularly considering the thermal profile and control over location-specific properties when scaling up WAAM applications.

Methods

Sample preparation

The composition (specified by vendor) for P91 steel (ER90S-B91, Euroweld, USA) and 740H superalloy (Special Metals Welding Products Co., USA) wires that were employed for the deposition of the designed alloy by mixing 90 wt.% P91 steel and 10 wt.% 740H alloy (named as 90 wt.% P91 alloy in following context) and the linear gradient build (Fig. 1) using WAAM are listed in Table 1. The diameter of the P91 steel and 740H superalloy wires were 0.9 and 1 mm, respectively. The fabrication of the linear gradient build involved the printing of a wall structure with 25 mm P91 steel on the bottom, 25 mm P91 to 740H alloy on the medium and 25 mm 740H alloy on the top Supplementary Fig. S4. We did not build the 740H close to the substrate since the lower thermal conductivity of 740H superalloy (10.2 W/mK) compared to P91 steel (26 W/mK) means the heat generated during deposition cannot dissipate effectively and will lead to crack formation³⁰. This WAAM printing task was carried out utilizing an ABB robotic platform at the RTX Technology Research Center. The WAAM system incorporated a Thermal Dynamics PWM300 plasma arc welding (PAW) torch and a twin wire feeder, both seamlessly integrated into a six-axis robot. During the fabrication process, purified argon gas was employed for plasma generation and as a shielding gas for the PAW torch, with a flow rate set at 1.2 liters per minute. Each layer in the additive manufacturing process was constructed using a square raster pattern with a pattern width of 11 mm and a step-over distance of 3 mm. As shown in the Supplementary Fig. S5, even-numbered layers followed a left-to-right square direction, while odd-numbered layers mirrored this pattern in a right-to-left direction.

Throughout the printing process, we ensured a consistent mass deposition rate of 0.9 kg/hr by continuously monitoring a precisely calibrated wire feeder. The feeder's controlled feed rate, along with the known material density and wire dimensions, allowed us to directly calculate and maintain the desired deposition rate within acceptable tolerances. The distance between the torch and the deposition point was set at 12 mm, while the wire was fed at an angle of 30 degrees. In order to achieve the desired composition gradient, the wire feed rates were adjusted based on the prescribed nominal composition, in conjunction with the appropriate current and travel speed settings as outlined in Table 2. The layer height varies due to P91, 740H, and their blends exhibit different properties and solidification behaviour. To prevent dilution from impacting the height of the build, an interpass temperature of 175 °C was meticulously maintained. Temperature was continuously monitored using an infrared pyrometer, and the dwell times between layers were dynamically adjusted to ensure that a new layer

Table 1 | Composition (in wt.%) of the P91 and 740H wires used for deposition in the WAAM process and the nominal composition (in wt.%) of 90 wt.% P91 alloy

Material	Composition (wt.%)												
	Al	C	Co	Cr	Cu	Fe	Mn	Mo	Nb	Ni	Ti	Si	V
P91	0.003	0.09	-	9.2	0.03	Bal.	0.45	0.91	0.052	0.4	-	0.26	0.21
740H	1.4	0.03	20.3	24.6	0.02	0.2	0.24	0.5	1.49	Bal.	1.5	0.1	-
90 wt.% P91	0.143	0.084	2.03	10.74	0.029	Bal.	0.429	0.869	0.196	5.322	0.15	0.244	0.189

was initiated only after the temperature had dropped below 175 °C. The mild steel (Fe-0.165C-0.6Mn-0.225Si, wt.%) substrate, with a thickness of approximately 13 mm, served as the foundation for this intricate linear gradient build.

In accordance with the computational design strategy outlined in this study, a wall sample was fabricated by blending 90 wt.% P91 steel with the 740H superalloy. The wire feed rates for the P91 steel and 740H superalloy wires were set at 2.83 m/min and 0.24 m/min. During the fabrication process, the average voltage was maintained at approximately 20.9 V; however, due to inherent process variations, this value fluctuated by several volts, and it represents an average observed across both the linear gradient and 90 wt.% P91 builds. To achieve the desired composition gradient and layer-specific properties, the current and travel speed settings were varied for different layers, as summarized in Table 2. To ensure proper adhesion to the substrate, the initial layer was subjected to high current and low travel speed, thereby facilitating complete bonding. Subsequently, the current was gradually reduced while the travel speed was adjusted accordingly for subsequent layers. This layer-by-layer approach ensured the integrity and structural integrity of the build. Similarly, an interpass temperature of 175 °C was also controlled to ensure consistency throughout this build.

Microstructure characterization and mechanical testing

Both gradient and 90 wt.% wall sample, produced via WAAM, underwent sectioning along the build direction (XZ plane and Z is the build direction) using electric discharge machining (EDM) facilitating subsequent characterization. To achieve optimal surface quality, the as-built sample was

embedded in a thermosetting resin and subjected to mechanical polishing. This process involved grinding the sample surface with SiC emery papers ranging from 800 to 1200 grit, followed by cloth polishing using diamond suspensions containing 3 and 1 µm particles. A final polishing step utilized silica suspension with 0.04 µm particles, ensuring a scratch-free, mirror-like surface finish. Observations of the as-polished surface were performed with a field emission gun (FEG) source-equipped FEI Scios Dual-Beam focused ion beam (FIB) - scanning electron microscope (SEM). Elemental compositions were ascertained via energy-dispersive spectroscopy (EDS) analysis using an OctaneElite EDAX system integrated with the SEM. To delve into the phase characteristics in greater detail, electron backscattered diffraction (EBSD) was employed, facilitated by the EDAX Hikari EBSD system attached to the SEM. The resulting EBSD scan data were subsequently analyzed utilizing TSL-OIM software version 8, enabling the reconstruction of the prior austenite grain size from the EBSD scans of the martensite matrix using ARPGE^{61,62}, employing the K-S orientation relationship⁶³. Hardness measurements were conducted on the as-polished XZ plane utilizing an automated Vicker's microhardness tester (AMH55 with LM310AT Microindenter, LECO Corporation, USA) employing a load of 300 grams and a dwell time of 10 s. To assess the hardness distribution along the sample's length in the 90 wt.% P91 build, approximately 600 indentations were performed along the build direction (Z direction) of the XZ plane. The space between each indent is 1 mm, which that is 10 times larger than the ASTM standard suggested value (3 times of the indent diagonal length) to avoid the hardening effects due to the neighboring indents. Tensile tests were conducted in accordance with ASTM E8/E8M, using subsize specimens extracted from the 90 wt.% sample, with the tensile axis aligned along the build direction. Testing was performed at room temperature using an MTS 880 universal testing machine with a 100 kN load capacity. Displacement measurements were recorded using a 25 mm extensometer, and the tests were conducted at a strain rate of 0.03 min⁻¹.

Table 2 | Printing parameters for linear-gradient and 90 wt.% P91 build fabricated using WAAM

Build type	Layer No.	P91 content (wt.%)	Current (A)	Travel speed (mm/s)	Wire feed (m/min)	
					P91	740H
Linear gradient	25–40	0	166	5	-	2.44
	23–24	10	166	5	0.31	2.19
	22	20	166	5	0.63	1.95
	21	30	166	5	0.94	1.70
	20	40	166	5	1.26	1.46
	19	50	166	5	1.57	1.22
	18	60	166	5	1.88	0.97
	17	70	166	5	2.20	0.73
	16	80	166	5	2.51	0.49
	13–15	90	166	5	2.83	0.24
	3–12	100	166	5	3.10	-
	2	100	200	4	2.90	-
	1	100	220	3.5	2.90	-
90 wt.% P91	6–62	90	166	5	2.83	0.24
	5	90	175	5	2.83	0.24
	4	90	195	5	2.83	0.24
	3	90	205	5	2.83	0.24
	2	90	215	4	2.83	0.24
	1	90	255	3.5	2.83	0.24

Modeling and genetic algorithm

The prediction models for porosity and hardness were developed using the gradient boosting ML algorithm⁶⁴ implemented with the Scikit-learn package⁶⁵. To optimize the model descriptor sets and reduce the number of features from all 32 features to avoid overfitting, GA⁶⁶ was employed. Unlike principal component analysis, GA preserves the physical interpretability of individual descriptors, and it is more efficient to explore the near-optimal feature sets than a brute-force search of 2³² possible subsets. The performance of the models was evaluated using 5-fold cross-validation⁶⁷ to identify the model with the highest accuracy and generalizability. The GA parameters used in the optimization process were listed in Table 3. For the two properties of interests, hardness and the porosity for three tracks with 145 indents per track were measured experimentally. The porosity was obtained using the Scikit-Image⁶⁸ package to analyze the SEM images around the hardness indents. For the model descriptors, the compositions around the indents were taken as the average around the four vertices of the square-shaped hardness indent using energy dispersive spectroscopy. The phase fractions, thermal expansion coefficient (TEC), heat capacity (Cp), freezing range (difference between solidus and liquidus temperatures), and latent heat at the solidus temperature were calculated using the TC-Python toolkit from Thermo-Calc software⁶⁹. Commercial thermodynamic databases for steel (TCFE10) and Ni-base superalloy (TCNI10) were used for thermodynamic property calculation^{70,71}. Configuration entropy was calculated using the equation: $R \sum_i^n x_i \ln x_i$, where R is the gas constant, x_i is the atomic fraction of element i , and n is the total number of elements. Total entropy is related to the temperature profile and matrix composition, which

Table 3 | Genetic Algorithm Parameter Settings

Population size	Crossing probability	Crossover independent probability	Mutation probability	Mutation independent probability	Maximum number of features	Tournament size
200	0.5	0.5	0.2	0.05	32	3

varies during solidification and is not considered as a materials descriptor for the ML model. Martensite start (M_s) temperature was calculated using a data-mining decision tree model available from literature⁷².

Disclaimer

This report was prepared as an account of work sponsored by an agency of the United States Government. Neither the United States Government nor any agency thereof, nor any of their employees, makes any warranty, express or implied, or assumes any legal liability or responsibility for the accuracy, completeness, or usefulness of any information, apparatus, product, or process disclosed, or represents that its use would not infringe privately owned rights. Reference herein to any specific commercial product, process, or service by trade name, trademark, manufacturer, or otherwise does not necessarily constitute or imply its endorsement, recommendation, or favoring by the United States Government or any agency thereof. The views and opinions of authors expressed herein do not necessarily state or reflect those of the United States Government or any agency thereof.

Data availability

The datasets used during the current study are available from the corresponding author on reasonable request.

Code availability

The underlying code for this study may be made available to qualified researchers on reasonable request from the corresponding author.

Received: 2 January 2025; Accepted: 24 March 2025;

Published online: 02 May 2025

References

- Zhang, Z. & Gu, G. X. Finite-Element-Based Deep-Learning Model for Deformation Behavior of Digital Materials. *Adv. Theory Simulations* **3**, 2000031 (2020).
- Jin, Z., Zhang, Z., Demir, K. & Gu, G. X. Machine Learning for Advanced Additive Manufacturing. *Matter* **3**, 1541–1556 (2020).
- George, E. P., Raabe, D. & Ritchie, R. O. High-entropy alloys. *Nat. Rev. Mater.* **4**, 515–534 (2019).
- Miracle, D., Majumdar, B., Wertz, K. & Gorsse, S. New strategies and tests to accelerate discovery and development of multi-principal element structural alloys. *Scr. Mater.* **127**, 195–200 (2017).
- Long, H., Mao, S., Liu, Y., Zhang, Z. & Han, X. Microstructural and compositional design of Ni-based single crystalline superalloys — A review. *J. Alloys Compd.* **743**, 203–220 (2018).
- Reed, R. C., Tao, T. & Warnken, N. Alloys-by-design: application to nickel-based single crystal superalloys. *Acta Mater.* **57**, 5898–5913 (2009).
- Chen, J. et al. A review on fundamental of high entropy alloys with promising high-temperature properties. *J. Alloys Compd.* **760**, 15–30 (2018).
- Rae, C. M. F. & Reed, R. C. The precipitation of topologically close-packed phases in rhenium-containing superalloys. *Acta Mater.* **49**, 4113–4125 (2001).
- Detroit, M. et al. Design and thermomechanical properties of a γ' precipitate-strengthened Ni-based superalloy with high entropy γ matrix. *J. Alloys Compd.* **792**, 550–560 (2019).
- Ghiringhelli, L. M., Vybiral, J., Levchenko, S. V., Draxl, C. & Scheffler, M. Big data of materials science: critical role of the descriptor. *Phys. Rev. Lett.* **114**, 105503 (2015).
- Li, Z., Ludwig, A., Savan, A., Springer, H. & Raabe, D. Combinatorial metallurgical synthesis and processing of high-entropy alloys. *J. Mater. Res.* **33**, 3156–3169 (2018).
- Marshall, A. et al. Combinatorial synthesis of high entropy alloys: Introduction of a novel, single phase, body-centered-cubic FeMnCoCrAl solid solution. *J. Alloys Compd.* **691**, 683–689 (2017).
- Kauffmann, A. et al. Combinatorial exploration of the high entropy alloy system Co-Cr-Fe-Mn-Ni. *Surf. Coatings Technol.* **325**, 174–180 (2017).
- Kuczka, W. et al. Studies of “sluggish diffusion” effect in Co-Cr-Fe-Mn-Ni, Co-Cr-Fe-Ni and Co-Fe-Mn-Ni high entropy alloys; determination of tracer diffusivities by combinatorial approach. *J. Alloys Compd.* **731**, 920–928 (2018).
- Wilson, P., Field, R. & Kaufman, M. The use of diffusion multiples to examine the compositional dependence of phase stability and hardness of the Co-Cr-Fe-Mn-Ni high entropy alloy system. *Intermetallics* **75**, 15–24 (2016).
- Zhao, J. -C. Combinatorial approaches as effective tools in the study of phase diagrams and composition–structure–property relationships. *Prog. Mater. Sci.* **51**, 557–631 (2006).
- Campbell, C. E., Zhao, J. -C. & Henry, M. F. Examination of Ni-base superalloy diffusion couples containing multiphase regions. *Mater. Sci. Eng. A* **407**, 135–146 (2005).
- Campbell, C. E., Zhao, J. -C. & Henry, M. F. Comparison of experimental and simulated multicomponent Ni-base superalloy diffusion couples. *J. Phase Equilibria Diffus.* **25**, 6–15 (2004).
- Wang, Z. et al. High throughput experiment assisted discovery of new Ni-base superalloys. *Scr. Mater.* **178**, 134–138 (2020).
- Haase, C., Tang, F., Wilms, M. B., Weisheit, A. & Hallstedt, B. Combining thermodynamic modeling and 3D printing of elemental powder blends for high-throughput investigation of high-entropy alloys – Towards rapid alloy screening and design. *Mater. Sci. Eng. A* **688**, 180–189 (2017).
- Borkar, T. et al. A combinatorial approach for assessing the magnetic properties of high entropy alloys: role of Cr in AlCo_xCr_{1-x}FeNi. *Adv. Eng. Mater.* **19**, 1700048 (2017).
- Li, M., Gazquez, J., Borisevich, A., Mishra, R. & Flores, K. M. Evaluation of microstructure and mechanical property variations in Al_xCoCrFeNi high entropy alloys produced by a high-throughput laser deposition method. *Intermetallics* **95**, 110–118 (2018).
- Welk, B. A., Gibson, M. A. & Fraser, H. L. A Combinatorial Approach to the Investigation of Metal Systems that Form Both Bulk Metallic Glasses and High Entropy Alloys. *JOM* **68**, 1021–1026 (2016).
- Sridar, S., Wang, X., Shabani, M., Klecka, M. A. & Xiong, W. Design of Graded Transition Interlayer for Joining Inconel 740H Superalloy with P91 Steel Using Wire-Arc Additive Manufacturing. in *TMS Annual Meeting & Exhibition* 755–772 (Springer, 2023).
- Agarwala, M., Bourell, D., Beaman, J., Marcus, H. & Barlow, J. Direct selective laser sintering of metals. *Rapid Prototyp. J.* **1.1**, 26–36 (1995).
- Lewis, G. K. & Schlienger, E. Practical considerations and capabilities for laser assisted direct metal deposition. *Mater. Des.* **21**, 417–423 (2000).
- Taminger, K. & Hafley, R. A. Electron beam freeform fabrication: a rapid metal deposition process. In 3rd annual automotive composites conference <https://ntrs.nasa.gov/citations/20040042496> (2003).
- Ding, J. et al. Thermo-mechanical analysis of Wire and Arc Additive Layer Manufacturing process on large multi-layer parts. *Comput. Mater. Sci.* **50**, 3315–3322 (2011).
- Sridar, S., Sargent, N., Wang, X., Klecka, M. A. & Xiong, W. Determination of Location-Specific Solidification Cracking Susceptibility for a Mixed Dissimilar Alloy Processed by Wire-Arc Additive Manufacturing. *Metals (Basel)*. **12**, 284 (2022).
- Sridar, S., Klecka, M. A. & Xiong, W. Interfacial characteristics of P91 steel-Inconel 740H bimetallic structure fabricated using wire-arc additive manufacturing. *J. Mater. Process. Technol.* **300**, 117396 (2022).
- Mazumder, J., Dutta, D., Kikuchi, N. & Ghosh, A. Closed loop direct metal deposition: art to part. *Opt. Lasers Eng.* **34**, 397–414 (2000).
- Wanjara, P., Brochu, M. & Jahazi, M. Electron beam freeforming of stainless steel using solid wire feed. *Mater. Des.* **28**, 2278–2286 (2007).
- DebRoy, T. et al. Additive manufacturing of metallic components – Process, structure and properties. *Prog. Mater. Sci.* **92**, 112–224 (2018).

34. Ding, D., Pan, Z., Cuiuri, D. & Li, H. A multi-bead overlapping model for robotic wire and arc additive manufacturing (WAAM). *Robot. Comput. Integr. Manuf.* **31**, 101–110 (2015).
35. Wang, F., Williams, S., Colegrove, P. & Antonysamy, A. A. Microstructure and Mechanical Properties of Wire and Arc Additive Manufactured Ti-6Al-4V. *Metall. Mater. Trans. A* **44**, 968–977 (2013).
36. Unocic, R. R. & DuPont, J. N. Process efficiency measurements in the laser engineered net shaping process. *Metall. Mater. Trans. B* **35**, 143–152 (2004).
37. Rännar, L., Glad, A. & Gustafson, C. Efficient cooling with tool inserts manufactured by electron beam melting. *Rapid Prototyp. J.* **13.3**, 128–135 (2007).
38. DuPont, J. N. & Marder, A. R. Thermal efficiency of arc welding processes. *Weld. Journal-Including Weld. Res. Suppl.* **74**, 406s (1995).
39. Yan, W. et al. Data-driven multi-scale multi-physics models to derive process–structure–property relationships for additive manufacturing. *Comput. Mech.* **61**, 521–541 (2018).
40. Wang, Z. et al. Uncertainty Quantification in Metallic Additive Manufacturing Through Physics-Informed Data-Driven Modeling. *JOM* **71**, 2625–2634 (2019).
41. Ouyang, R., Curtarolo, S., Ahmetcik, E., Scheffler, M. & Ghiringhelli, L. M. SISSO: A compressed-sensing method for identifying the best low-dimensional descriptor in an immensity of offered candidates. *Phys. Rev. Mater.* **2**, 83802 (2018).
42. Goldberg, D. E. *Genetic Algorithms in Search, Optimization and Machine Learning*. (Addison-Wesley Longman Publishing Co., Inc., USA, 1989).
43. Lukas, H., Fries, S. G. & Sundman, B. *Computational Thermodynamics: The Calphad Method*. (Cambridge University Press, 2007).
44. Li, K., Klecka, M. A., Chen, S. & Xiong, W. Wire-arc additive manufacturing and post-heat treatment optimization on microstructure and mechanical properties of Grade 91 steel. *Addit. Manuf.* **37**, 101734 (2021).
45. Sridar, S., Ladinis Pizano, L. F., Klecka, M. A. & Xiong, W. Achieving High Strength and Creep Resistance in Inconel 740H Superalloy through Wire-Arc Additive Manufacturing and Thermodynamic-Guided Heat Treatment. *Materials* **16** at <https://doi.org/10.3390/ma16196388> (2023).
46. Panwisawas, C., Gong, Y., Tang, Y. T., Reed, R. C. & Shinjo, J. Additive manufacturability of superalloys: Process-induced porosity, cooling rate and metal vapour. *Addit. Manuf.* **47**, 102339 (2021).
47. Sabzi, H. E. et al. Controlling crack formation and porosity in laser powder bed fusion: Alloy design and process optimisation. *Addit. Manuf.* **34**, 101360 (2020).
48. Knapp, G. L. et al. Building blocks for a digital twin of additive manufacturing. *Acta Mater.* **135**, 390–399 (2017).
49. Khanzadeh, M. et al. In-situ monitoring of melt pool images for porosity prediction in directed energy deposition processes. *IJSE Trans.* **51**, 437–455 (2019).
50. Sui, S. et al. Microstructures and stress rupture properties of pulse laser repaired Inconel 718 superalloy after different heat treatments. *J. Alloys Compd.* **770**, 125–135 (2019).
51. Ludwig, A. Discovery of new materials using combinatorial synthesis and high-throughput characterization of thin-film materials libraries combined with computational methods. *npj Comput. Mater.* **5**, 70 (2019).
52. Osada, T. et al. Optimum microstructure combination for maximizing tensile strength in a polycrystalline superalloy with a two-phase structure. *Acta Mater.* **61**, 1820–1829 (2013).
53. Pandey, C., Giri, A. & Mahapatra, M. M. Evolution of phases in P91 steel in various heat treatment conditions and their effect on microstructure stability and mechanical properties. *Mater. Sci. Eng. A* **664**, 58–74 (2016).
54. Hu, R. et al. Inconel 740H Prepared by Additive Manufacturing: Microstructure and Mechanical Properties. *Metals* **14** at <https://doi.org/10.3390/met14070809> (2024).
55. Athira, K. S. & Chatterjee, S. Effect of keyhole gas tungsten arc welding and post-welding heat treatment on microstructure and hardness of inconel 740H. *J. Mater. Eng. Perform.* **33**, 12452–12466 (2024).
56. Sridar, S. et al. 755–772 (Springer Nature Switzerland, Cham, 2023).
57. Bourell, D. et al. Materials for additive manufacturing. *CIRP Ann.* **66**, 659–681 (2017).
58. Kim, F. H., Moylan, S. P., Garboczi, E. J. & Slotwinski, J. A. Investigation of pore structure in cobalt chrome additively manufactured parts using X-ray computed tomography and three-dimensional image analysis. *Addit. Manuf.* **17**, 23–38 (2017).
59. Dantzig, J. A. & Rappaz, M. *Solidification: -Revised & Expanded*. (EPFL press, 2016).
60. Leigh, D. K., Bourell, D. L. & Beaman Jr, J. J. Effect of in-plane voiding on the fracture behavior of laser sintered polyamide. in *International Symposium on Flexible Automation* 45110 411–417 (American Society of Mechanical Engineers, 2012).
61. Cayron, C. ARPGE: a computer program to automatically reconstruct the parent grains from electron backscatter diffraction data. *J. Appl. Crystallogr.* **40**, 1183–1188 (2007).
62. Cayron, C., Artaud, B. & Briottet, L. Reconstruction of parent grains from EBSD data. *Mater. Charact.* **57**, 386–401 (2006).
63. Kurdjumow, G. & Sachs, G. Über den mechanismus der stahlhärtung. *Zeitschrift für Phys.* **64**, 325–343 (1930).
64. Friedman, J. H. Greedy function approximation: a gradient boosting machine. *Ann. Stat.* **29**, 1189–1232 (2001).
65. Pedregosa, F. et al. Scikit-learn: Machine learning in Python. *J. Mach. Learn. Res.* **12**, 2825–2830 (2011).
66. Calzolari, M. manuel-calzolari/sklearn-genetic: sklearn-genetic 0.4.1. (2021) <https://doi.org/10.5281/ZENODO.4661248>.
67. Kohavi, R. A study of cross-validation and bootstrap for accuracy estimation and model selection. in *Ijcai* 14 1137–1145 (Montreal, Canada, 1995).
68. van der Walt, S. et al. scikit-image: image processing in Python. *PeerJ* **2**, e453 (2014).
69. Andersson, J. -O., Helander, T., Höglund, L., Shi, P. & Sundman, B. Thermo-Calc & DICTRA, computational tools for materials science. *Calphad* **26**, 273–312 (2002).
70. Shin, D., Yamamoto, Y., Brady, M. P., Lee, S. & Haynes, J. A. Modern data analytics approach to predict creep of high-temperature alloys. *Acta Mater.* **168**, 321–330 (2019).
71. Shen, C. et al. Physical metallurgy-guided machine learning and artificial intelligent design of ultrahigh-strength stainless steel. *Acta Mater.* **179**, 201–214 (2019).
72. Agrawal, A., Saboo, A., Xiong, W., Olson, G. & Choudhary, A. Martensite Start Temperature Predictor for Steels Using Ensemble Data Mining. *2019 IEEE Int. Conf. Data Sci. Adv. Anal.* 521–530 (2019).

Acknowledgements

The authors gratefully acknowledge the financial support from the National Energy Technology Laboratory, Department of Energy, United States under the award number DE-FE0031637.

Author contributions

X.W. conducted all calculations, curated and analyzed the data, visualized the results, and significantly contributed to writing the manuscript. S.S. carried out the characterization and testing, participated in result discussions, and contributed to manuscript writing. M.K. prepared the samples and contributed to the discussion of the results. W.X.

conceptualized and supervised the work, secured funding, and was actively involved in the analysis and discussion. All authors reviewed and approved the final manuscript.

Competing interests

The authors declare no competing interests.

Additional information

Supplementary information The online version contains supplementary material available at

<https://doi.org/10.1038/s44334-025-00028-x>.

Correspondence and requests for materials should be addressed to Wei Xiong.

Reprints and permissions information is available at <http://www.nature.com/reprints>

Publisher's note Springer Nature remains neutral with regard to jurisdictional claims in published maps and institutional affiliations.

Open Access This article is licensed under a Creative Commons Attribution 4.0 International License, which permits use, sharing, adaptation, distribution and reproduction in any medium or format, as long as you give appropriate credit to the original author(s) and the source, provide a link to the Creative Commons licence, and indicate if changes were made. The images or other third party material in this article are included in the article's Creative Commons licence, unless indicated otherwise in a credit line to the material. If material is not included in the article's Creative Commons licence and your intended use is not permitted by statutory regulation or exceeds the permitted use, you will need to obtain permission directly from the copyright holder. To view a copy of this licence, visit <http://creativecommons.org/licenses/by/4.0/>.

© The Author(s) 2025